

Virtual Impedance Design Considerations for Virtual Synchronous Machines in Weak Grids

Alberto Rodríguez-Cabero[✉], Javier Roldán-Pérez[✉], Member, IEEE, and Milan Prodanovic[✉], Member, IEEE

Abstract—Most renewable energy sources (RESs) are interfaced to electricity grids via voltage-source converters (VSCs). To facilitate the integration, the controllers based on the emulation of synchronous generators have been increasingly used. This control technique is commonly referred to as Virtual Synchronous Machine (VSM) and recent studies have shown that VSMs are sensitive to variations in the network parameters if no countermeasures in form of virtual impedances are applied. However, a thorough and comprehensive methodology for the design of virtual impedance for VSMs has not been yet presented in the literature and the development of such procedure for the VSMs connected to weak grids is the principal objective of this paper. Each dynamic element of the VSM is modeled and all of them are then joined together forming a state-space model. The eigenvalue and singular value decomposition (SVD) analyzes were used then to evaluate the impact of the grid model and the virtual impedance on the VSM dynamics. From these results, a practical guide to design both the VSM and the virtual impedance parameters was proposed. All the theoretical developments were validated experimentally on a 15-kVA prototype of a VSM connected to a weak grid.

Index Terms—Control system, distributed power generation, power conversion, power system modeling, stability.

NOMENCLATURE

Variables

i_1	Converter-side current.
i_2	Grid-side current.
e_S	Voltage-source converter (VSC) output voltage.
v_S	Virtual Synchronous Machine (VSM) command voltage.
v_{pcc}	Point of common coupling (PCC) voltage.
v_g	Ideal grid voltage.
ω_s, θ_s	Synchronous frequency and angle.
ω_s^*	Synchronous frequency set point.
T_m, T_e	Mechanical and electromechanical torques.
ψ_v	Virtual flux.
p, q	Active and reactive power delivered to the grid.
P^*, Q^*	Active and reactive power set points.

Manuscript received September 21, 2018; revised February 20, 2019; accepted April 14, 2019. Date of publication April 18, 2019; date of current version May 6, 2020. This work was supported by the Regional Government of Madrid, Spain, through the research project PROMINT-CM under Grant P2018/EMT4366. Recommended for publication by Associate Editor Dehong Xu. (Corresponding author: Alberto Rodríguez-Cabero.)

The authors are with the Electrical Systems Unit, IMDEA Energy Institute, 28935 Madrid, Spain (e-mail: alberto.rodriguez@imdea.org; javier.roldan@imdea.org; milan.prodanovic@imdea.org).

Color versions of one or more of the figures in this article are available online at <http://ieeexplore.ieee.org>.

Digital Object Identifier 10.1109/JESTPE.2019.2912071

Parameters

J_v	Moment of inertia.
K_Q	Reactive power controller integral gain.
D_P, D_Q	Active and reactive power droop gains.
R_V, L_V	Virtual resistance and inductance.

I. INTRODUCTION

A. Motivation and Incitement

The renewable energy source (RES) integration to electricity networks is the main driving force behind the changes in the power system operation paradigm. In this scenario, RES and other elements connected to the grid by using power electronics converters represent a sizeable share of generation units. For this reason, system operators are requesting grid voltage and frequency support from these devices [1]. In many cases, RES is located in remote locations and they have to be connected to the main grid by using long distribution lines creating parts of the network usually defined as “weak grids” [2]. These weak connections introduce critical issues to the power system operation by making the regulation of voltage profiles more difficult to and by limiting the power transmission capacity [3]. Moreover, high penetration of RES based on power electronics converters can lead to interactions between them and other network elements [4].

B. Literature Review

Several authors have studied the problem of RES integration to microgrids and weak grids from the network point of view, proposing hierarchical control schemes (primary, secondary, and tertiary controllers), and analyzing their dynamic properties [5]–[7]. Typically, these control strategies include a local controller (current and/or voltage) and a primary controller based on the well-known droop method [8]–[10]. Then, secondary and tertiary regulations are achieved by using controllers that work on a different time scale. These high-level controllers can be implemented in a centralized or decentralized manner [11]–[14].

A recent concept to simplify the integration of voltage-source converters (VSCs) from the primary controller point of view is to emulate the dynamics of conventional generators with their control system [15]. This control technique is commonly known as Virtual Synchronous Machine (VSM) and it mimics the electromechanical transient response of a synchronous generator. VSMs are

an attractive approach for a smooth integration of RES to power systems since they are inherently designed to operate together with synchronous generators. However, VSMs are nonlinear and this fact makes them more challenging to design and analyze. Moreover, closed-loop stability of VSMs must be guaranteed over all possible scenarios and operating conditions such as a weak grid. For example, Dong and Chen [16] studied the frequency oscillations caused by VSMs under certain grid conditions, e.g., single phase-to-earth faults. A solution to damp oscillations was provided by using an auxiliary control loop that adjusted the VSM transient response. Ma and Zhong [17] proposed a control strategy based on VSMs for variable-speed wind turbines connected to the grid via back-to-back (BTB) converters. As a result, the BTB converter was equivalent to a generator-motor-generator system, and it was possible to guarantee an adequate operation of the wind turbine. Aouini *et al.* [18] proposed a VSM control strategy for an HVdc-VSC link that interconnected two weak grids. Transient stability issues of the weak grids were considered to design of VSMs parameters. The VSM alternative was compared to the standard space-vector control, revealing that VSMs provided better transient performance and stability indices. Natarajan and Weiss [19] proposed five modifications to the conventional VSM controller based on virtual impedances. Stability and performance improved, but stability issues for weak grid applications were not studied. Chen *et al.* [20] proposed a VSM for the integration of dc-microgrids into the main ac grid. A VSM was implemented on top of a dual-droop control in order to manage the power transferred between the two grids. Shuai *et al.* [21] studied stability limits of a distribution network that included VSMs. A small-signal model was developed and the influence of droop coefficients on the system stability was analyzed by using the eigenvalue analysis and the bifurcation theory. Roldán-Pérez *et al.* [22] proposed an alternative VSM formulation and a systematic approach to design its parameters. The VSM discretization was also studied and several implementation issues were solved. This literature review revealed that there are many research studies evaluating the potential use of VSMs. Also, several authors already studied the grid influence on the stability and transient performance of VSMs. However, a systematic design of the VSM parameters under weak grid conditions has not been yet addressed and this represents the main objective of the study provided in this paper.

In recent years, the virtual impedance control technique has gained popularity since it offers a simple way of modifying the output impedance of grid-connected VSCs [23]. Virtual impedances are mainly used to improve power-sharing capabilities of converters in microgrids [24], [25], although they can also be used to improve performance under grid faults [26] and to deal with power quality issues [27]. The virtual impedance has already been applied to VSMs in order to improve their power-sharing capabilities. For example, Suul *et al.* [28] proposed a single-phase battery charger for electric vehicles controlled as a VSM. Internal current and voltage controllers were used and an additional virtual impedance is added. The virtual impedance was necessary to guarantee a stable

operation under stiff grid conditions when more than one VSM is operated in parallel. Piya and Karimi-Ghartemani [29] analyzed the stability properties of a VSM showing that stability margins were directly related to the presence of external passive elements. A virtual resistor was proposed as an effective solution to improve stability margins. Several authors have highlighted the benefits of virtual impedances for VSMs. However, a detailed analysis tools and control design procedure have not been addressed yet and represent the main goal of this paper.

C. Principal Contributions

With an objective to improve the stability margins in VSM applications across a range of different grid impedance scenarios, this paper proposes a novel method to design the VSM parameters with added virtual impedance. In order to do so, a small-signal model of the VSM with the virtual impedance is derived and then comprehensively studied.

Moreover, the impact of the virtual impedance and the grid model on the VSM stability properties is evaluated by using the system eigenvalues and singular values (SVs). Variations of the grid model and the VSM control parameters are all taken into consideration and the obtained results are critically compared. Based on the results of the evaluation, a practical guide to design of the VSM and virtual impedance parameters is presented.

The small-signal model and the proposed control design procedure are validated in simulation and then also by using a experimental test environment—a 15-kVA VSM converter prototype connected to a configurable weak grid.

II. APPLICATION AND CONTROL SYSTEM OVERVIEW

A. Virtual Synchronous Machine Application

Fig. 1 shows the electrical and control system diagram of the VSM that will be studied in this paper [22]. The system consists of a VSC connected to the ac grid via an *LCL* filter and it emulates the dynamic response of a synchronous generator. The converter-side inductance is L_1 , the grid-side inductance is L_2 , and the filter capacitor is C_f . The grid is modeled as an equivalent impedance (Z_g) representing the power network topology and dynamic properties of all power converters connected in its proximity. As an example, Agorreta *et al.* [30] showed that when N identical converters are connected in parallel to the grid and operated in a coordinated way, the equivalent impedance seen by each converter is the nominal grid impedance multiplied by N . In this paper, it is assumed that the power converter is connected to the grid via a long line producing the equivalent grid impedance $Z_{g(s)} \approx R_g + L_{gs}$. The modeling approach proposed in this paper is generic and can be applied to any arbitrary complex grid model. A synchronous reference frame (SRF) synchronized with the q -axis component of VSM internal voltage (v_S) is used for the controller implementation.

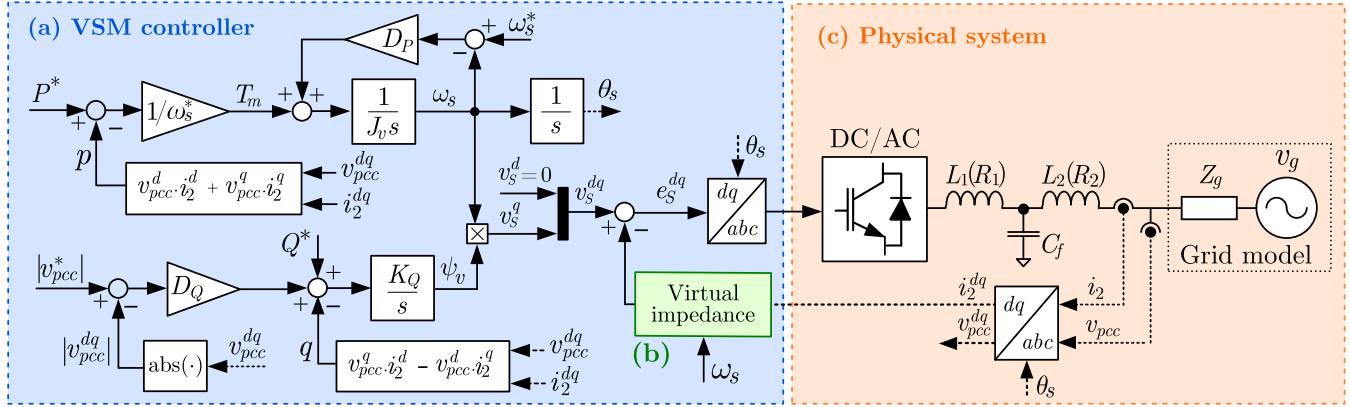


Fig. 1. Electrical and control system diagram of a power electronics converter connected to the grid. The converter emulates the dynamics of a synchronous machine.

B. VSM Control System Overview

The VSM formulation in an SRF is summarized [22] and depicted in Fig. 1. The VSM virtual shaft can be modeled with

$$J_v \cdot d\omega_s/dt = T_m - T_e + \underbrace{D_P(\omega_s^* - \omega_s)}_{\text{Frequency droop}} \quad (1)$$

where ω_s is the synchronous frequency and ω_s^* is its set point, T_m and T_e are mechanical and electromechanical torques, respectively, D_P is the active power droop gain, and J_v is the virtual moment of inertia. The torques can be computed as

$$T_m = P^*/\omega_s, \quad T_e = p/\omega_s \quad (2)$$

where p is the instantaneous active power and P^* is its set point. As shown in [15], the relative difference between ω_s and ω_s^* is small in grid applications. Therefore, by assuming that $\omega_s \approx \omega_s^*$, the relation between torques and powers in (2) becomes linear. Therefore, the mechanical and the electromechanical torques can be calculated in terms of the instantaneous active power (p) and its set point (P^*), respectively: $T_e = p/\omega_s^*$ and $T_m = P^*/\omega_s^*$. Hence, the virtual shaft equation can be rewritten as

$$d\omega_s/dt = K_{J\omega}(P^* - p) + K_{DJ}(\omega_s^* - \omega_s) \quad (3)$$

$$d\theta_s/dt = \omega_s \quad (4)$$

where $K_{J\omega} = 1/(J_v \omega_s^*)$ and $K_{DJ} = D_P/J_v$.

Reactive power is controlled by using the VSM virtual flux (ψ_v) that is computed as

$$d\psi_v/dt = K_Q(Q^* - q + \underbrace{D_Q \cdot (|v_{pcc}^*| - |v_{pcc}^d|)}_{\text{Voltage droop}}) \quad (5)$$

where q is the instantaneous reactive power, Q^* is the reactive power set point, K_Q is the reactive power controller integral gain, D_Q is the reactive power droop gain, $|v_{pcc}^d|$ is the instantaneous voltage modulus at the point of common coupling (PCC), and $|v_{pcc}^*|$ is its set-point value. The VSM d -axis internal voltage is set to zero ($v_S^d = 0$), while the q -axis component is

$$v_S^q = \psi_v \omega_s. \quad (6)$$

In this paper, the grid-side active and reactive powers are used as feedback signals and the voltage at the PCC (v_{pcc}^d) represents the output voltage of the VSM [19]. By using the power invariant Park's transform, active and reactive powers can be calculated as in [31]

$$p = v_{pcc}^d i_2^d + v_{pcc}^q i_2^q \quad (7)$$

$$q = v_{pcc}^q i_2^d - v_{pcc}^d i_2^q \quad (8)$$

where i_2 is the grid-side current.

C. Virtual Impedance for VSMs

Fig. 2(a) shows an equivalent block diagram of the virtual impedance concept for VSMs [19], [32]. The VSM output voltage (e_S) is generated by adding an additional feedback loop to the VSM command voltage (v_S) that includes a low-pass filter (LPF) and the virtual impedance transfer function ($Z_V(s)$). The virtual impedance can be defined as follows:

$$Z_V(s) = R_V + L_V s \quad (9)$$

where R_V and L_V are the virtual resistance and inductance, respectively, and $V_S(s)$ and $E_S(s)$ are the Laplace transformations of $v_S(t)$ and $e_S(t)$, respectively. Transfer function $P(s)$ models the LCL filter, linking the VSC output voltage and the grid-side current. In practice, pure derivative terms are rarely used to implement virtual impedances as they would amplify noise. Instead, an algebraic approximation at the synchronous frequency (ω_s) can be used [23]. This approximation is obtained by substituting $s = j\omega_s$ in (9). Fig. 2(b) shows a block diagram that represents the algebraic approximation of the virtual impedance. One should note that this is a steady-state approximation and is equivalent to (9) only at the synchronous frequency. By using this formulation, the synchronous frequency is needed in the virtual impedance to adjust the virtual reactance, $X_V = L_V \omega_s$.

The direct use of the algebraic approximation is not recommended in weak grids since it can amplify noise and generate high-frequency stability problems [23]. Therefore, a filtered version of i_2^{dq} (i_2^{dq-f}) is added to the virtual impedance loop. A first-order LPF is applied to each of the components

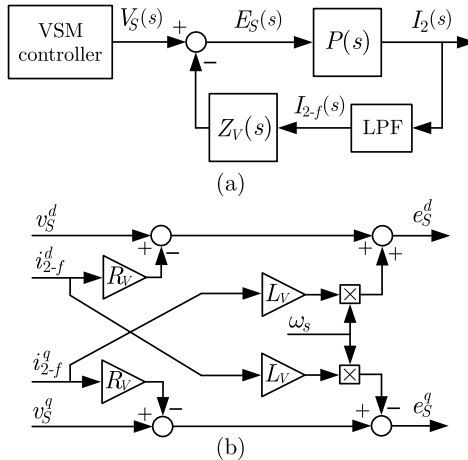


Fig. 2. Control diagram of (a) VSM with a virtual impedance and (b) algebraic-type virtual impedance.

of i_2^{dq} before applying the virtual impedance. The state-space representation of the two LPFs can be written as

$$\frac{d}{dt}i_{2-f}^d = \omega_c \cdot (i_2^d - i_{2-f}^d) \quad (10)$$

$$\frac{d}{dt}i_{2-f}^q = \omega_c \cdot (i_2^q - i_{2-f}^q) \quad (11)$$

where ω_c is the cutoff frequency of the LPF.

D. Small-Signal Modeling Approach

In this paper, all the system elements are aggregated in a state-space model referred to a common reference frame (DQ) that is synchronized to the ideal grid voltage (v_g) shown in Fig. 1 [33]. The VSM has its own reference frame (dq) synchronized to the VSM command voltage (v_S). The VSM equations are referred to the DQ reference frame by using the following rotation matrix:

$$\begin{bmatrix} f^D \\ f^Q \end{bmatrix} = \underbrace{\begin{bmatrix} \cos \theta & -\sin \theta \\ \sin \theta & \cos \theta \end{bmatrix}}_{R(\theta)} \begin{bmatrix} f^d \\ f^q \end{bmatrix} \quad (12)$$

where θ is the angle between the reference frames, while f^D and f^{dq} represent dq -components of currents and voltages.

E. Singular Value Decomposition

Consider the following state-space representation of a linear time-invariant system:

$$\dot{x}(t) = Ax(t) + Bu(t) \quad (13)$$

$$y(t) = Cx(t) + Du(t) \quad (14)$$

where A , B , C , and D are the system state-space matrices. The transfer-function matrix of the aforementioned state-space model can be calculated as [34], [35]

$$G(s) = C(sI - A)^{-1}B \quad (15)$$

where I is the identity matrix. For any given frequency, the SV decomposition (SVD) can be calculated as follows:

$$G(j\omega) = U(j\omega)\Sigma(j\omega)V^T(j\omega) \quad (16)$$

where $\Sigma(\omega)$ are the SV, and $U(j\omega)$ and $V(j\omega)$ are the left and right singular vectors of $G(j\omega)$, respectively [34], [35].

III. VSM SMALL-SIGNAL MODELING

A. LCL Filter Model

One possible small-signal model of a LCL filter can be written as follows [36]:

$$\frac{d}{dt} \Delta x_f^{dq} = A_f \Delta x_f^{dq} + B_f^S \Delta e_S^{dq} + B_f^{pcc} \Delta v_{pcc}^{dq} + B_f^\omega \Delta \omega_s \quad (17)$$

$$\Delta i_2^{dq} = C_{L2} \Delta x_f^{dq} \quad (18)$$

with

$$A_f = \begin{bmatrix} -\frac{R_1}{L_1} & \Omega_s & 0 & 0 & 0 & 0 \\ -\Omega_s & -\frac{R_1}{L_1} & 0 & 0 & 0 & 0 \\ 0 & 0 & -\frac{1}{C_f} & \Omega_s & 0 & 0 \\ 0 & 0 & -\Omega_s & -\frac{1}{C_f} & 0 & 0 \\ 0 & 0 & 0 & 0 & -\frac{R_2}{L_2} & \Omega_s \\ 0 & 0 & 0 & 0 & -\Omega_s & -\frac{R_2}{L_2} \end{bmatrix} \quad (19)$$

$$B_f^S = \begin{bmatrix} \frac{1}{L_1} & 0 \\ 0 & \frac{1}{L_1} \\ 0 & 0 \\ 0 & 0 \\ 0 & 0 \\ 0 & 0 \end{bmatrix}, \quad B_f^{pcc} = \begin{bmatrix} 0 & 0 \\ 0 & 0 \\ 0 & 0 \\ 0 & 0 \\ -\frac{1}{L_2} & 0 \\ 0 & -\frac{1}{L_2} \end{bmatrix}, \quad B_f^\omega = \begin{bmatrix} I_2^d \\ I_2^q \\ V_f^d \\ V_f^q \\ I_2^d \\ I_2^q \end{bmatrix} \quad (20)$$

where the symbol “ Δ ” stands for the incremental operator, $C_{L2} = [0^{2 \times 2} \ 0^{2 \times 2} \ I^{2 \times 2}]$, $\Delta x_f^{dq} = [i_1^{dq} \ v_C^{dq} \ i_2^{dq}]^T$, v_C is the capacitor voltage, i_1 is the converter-side current, and i_2 is the grid-side current. In this paper, upper case Latin and Greek symbols stand for “operating point.”

B. Modeling of the Power Calculation

The instantaneous active and reactive powers are computed by using the nonlinear equations (7) and (8), which can be linearized around the operating point, yielding

$$\Delta p = V^P \Delta i_2^{dq} + I^P \Delta v_{pcc}^{dq} \quad (21)$$

$$\Delta q = V^Q \Delta i_2^{dq} + I^Q \Delta v_{pcc}^{dq} \quad (22)$$

with

$$V^P = [V_{pcc}^d \ V_{pcc}^q], \quad V^Q = [V_{pcc}^q \ -V_{pcc}^d] \quad (23)$$

$$I^P = [I_2^d \ I_2^q], \quad I^Q = [-I_2^q \ I_2^d] \quad (24)$$

where V_{pcc}^{dq} and I_2^{dq} are the operating points—PCC voltage and the grid-side current, respectively.

C. Modeling of the Voltage Modulus Calculation

The instantaneous value of the PCC voltage modulus can be computed as

$$|v_{pcc}^{dq}| = \sqrt{(v_{pcc}^d)^2 + (v_{pcc}^q)^2}. \quad (25)$$

By linearizing (25) around the operating point

$$|\Delta v_{pcc}^{dq}| = M_V \Delta v_{pcc}^{dq} \quad (26)$$

where M_V is the following row vector:

$$M_V = \left(1/\sqrt{(V_{pcc}^d)^2 + (V_{pcc}^q)^2}\right) \cdot [V_{pcc}^d \quad V_{pcc}^q]. \quad (27)$$

D. Virtual Impedance and Low-Pass Filter Model

The VSC output voltage (e_S^{dq}) is computed by adding the VSM command voltage (v_S^{dq}) and the virtual impedance contribution, yielding

$$e_S^d = v_S^d - R_V i_{2-f}^d + L_V \omega_s i_{2-f}^q \quad (28)$$

$$e_S^q = v_S^q - R_V i_{2-f}^q - L_V \omega_s i_{2-f}^d. \quad (29)$$

By linearizing (28) and (29) around the operating point

$$\begin{aligned} \Delta e_S^{dq} = \Delta v_S^{dq} + \underbrace{\begin{bmatrix} -R_V & L_V \Omega_s \\ -L_V \Omega_s & -R_V \end{bmatrix}}_{D_I} \Delta i_{2-f}^{dq} \\ + \begin{bmatrix} L_V I_{2-f}^q \\ -L_V I_{2-f}^d \end{bmatrix} \Delta \omega_s \end{aligned} \quad (30)$$

where Ω_s is the operating point of the synchronous frequency. The dynamic equations of the LPFs (10) and (11) are already linear and the small-signal model can be obtained by substituting i_2^{dq} and i_{2-f}^{dq} by their small-signal representations Δi_2^{dq} and Δi_{2-f}^{dq} . Therefore,

$$\frac{d}{dt} \Delta i_{2-f}^d = \omega_c \cdot (\Delta i_2^d - \Delta i_{2-f}^d) \quad (31)$$

$$\frac{d}{dt} \Delta i_{2-f}^q = \omega_c \cdot (\Delta i_2^q - \Delta i_{2-f}^q). \quad (32)$$

E. VSM Control System Model

The linearized version of the VSM equations (3)–(5) is

$$\frac{d}{dt} \Delta \omega_s = K_{J\omega} (\Delta P^* - \Delta p) + K_{DJ} (\Delta \omega_s^* - \Delta \omega_s) \quad (33)$$

$$\frac{d}{dt} \Delta \psi_v = K_Q (\Delta Q^* - \Delta q + D_Q (|\Delta v_{pcc}^*| - |\Delta v_{pcc}^{dq}|)) \quad (34)$$

$$\frac{d}{dt} \Delta \theta_s = \Delta \omega_s. \quad (35)$$

Also, the q -axis component of the VSM command voltage (6) can be linearized as follows:

$$\Delta v_S^q = \Psi_v \Delta \omega_s + \Omega_s \Delta \psi_v \quad (36)$$

where Ψ_v is the operating point of the virtual flux. By substituting (21) into (33), (22) and (26) into (34), (36) into (30), and aggregating the resulting equations with (31) and (32),

the linearized state-space model of the VSM control system with virtual impedance is obtained as

$$\begin{aligned} \frac{d}{dt} \Delta x_c = A_c \Delta x_c + B_c^i \Delta i_2^{dq} + B_c^{pcc} \Delta v_{pcc}^{dq} \\ + B_c^{|v|} |\Delta v_{pcc}^*| + B_c^\omega \Delta \omega_s^* + B_c^{PQ} \Delta P Q^* \end{aligned} \quad (37)$$

$$\begin{bmatrix} \Delta e_S^{dq} \\ \Delta \omega_s \\ \Delta \theta_s \end{bmatrix} = \begin{bmatrix} C_c^S \\ C_c^\omega \\ C_c^\theta \end{bmatrix} \Delta x_c \quad (38)$$

with

$$A_c = \begin{bmatrix} -1 & 0 & 0 & 0 & 0 \\ 0 & 0 & 0 & 0 & 0 \\ 1 & 0 & 0 & 0 & 0 \\ 0 & 0 & 0 & -\omega_c & 0 \\ 0 & 0 & 0 & 0 & -\omega_c \end{bmatrix}, \quad B_c^i = \begin{bmatrix} -K_{J\omega} V^P \\ -K_Q V^Q \\ 0 & 0 \\ \omega_c & 0 \\ 0 & \omega_c \end{bmatrix} \quad (39)$$

$$B_c^\omega = \begin{bmatrix} K_{DJ} \\ 0 \\ 0 \\ 0 \end{bmatrix}, \quad B_c^{pcc} = \begin{bmatrix} -K_{J\omega} I^P \\ K_Q D_Q M_V - K_{J\omega} I^Q \\ 0 & 0 \\ 0 & 0 \\ 0 & 0 \end{bmatrix} \quad (40)$$

$$B_c^{|v|} = \begin{bmatrix} 0 \\ K_Q D_q \\ 0 \\ 0 \\ 0 \end{bmatrix}, \quad B_c^{PQ} = \begin{bmatrix} K_{J\omega} & 0 \\ 0 & K_Q \\ 0 & 0 \\ 0 & 0 \\ 0 & 0 \end{bmatrix} \quad (41)$$

$$C_c^S = \begin{bmatrix} L_V I_{2-f}^q & 0 & 0 & -R_V & L_V \Omega_s \\ \Psi_v - L_V I_{2-f}^d & \Omega_s & 0 & -L_V \Omega_s & -R_V \end{bmatrix} \quad (42)$$

$$C_c^\omega = [1 \ 0 \ 0 \ 0 \ 0] \quad (43)$$

$$C_c^\theta = [0 \ 0 \ 1 \ 0 \ 0] \quad (44)$$

where $\Delta x_c = [\Delta \omega_s \ \Delta \psi_v \ \Delta \theta_s \ \Delta i_{2-f}^d \ \Delta i_{2-f}^q]^T$, $\Delta P Q^* = [\Delta P^* \ \Delta Q^*]^T$.

F. Aggregated VSM Model

Fig. 3 shows the VSM small-signal model obtained by merging the LCL filter model in (17) and (18) with the control system model in (37) and (38). The VSM input and output variables are v_{pcc}^{dq} and i_2^{dq} , respectively, and they have to be referred to the DQ -frame in order to connect the VSM to the power system model. By linearizing the rotation matrix (12), the required equations are

$$\Delta i_2^{DQ} = R_S \Delta i_2^{dq} + R_C \Delta \theta_s \quad (45)$$

$$\Delta v_{pcc}^{dq} = R_S^{-1} \Delta v_{pcc}^{DQ} + R_V \Delta \theta_s \quad (46)$$

with

$$R_S = \begin{bmatrix} \cos \Theta & -\sin \Theta \\ \sin \Theta & \cos \Theta \end{bmatrix} \quad (47)$$

$$R_C = \begin{bmatrix} -I_2^d \sin \Theta - I_2^q \cos \Theta \\ +I_2^d \cos \Theta - I_2^q \sin \Theta \end{bmatrix} \quad (48)$$

$$R_V = \begin{bmatrix} -V_{pcc}^d \sin \Theta + V_{pcc}^q \cos \Theta \\ -V_{pcc}^d \cos \Theta - V_{pcc}^q \sin \Theta \end{bmatrix} \quad (49)$$

where Θ is the angle between the dq and the DQ reference frames at the operating point [33], [35].

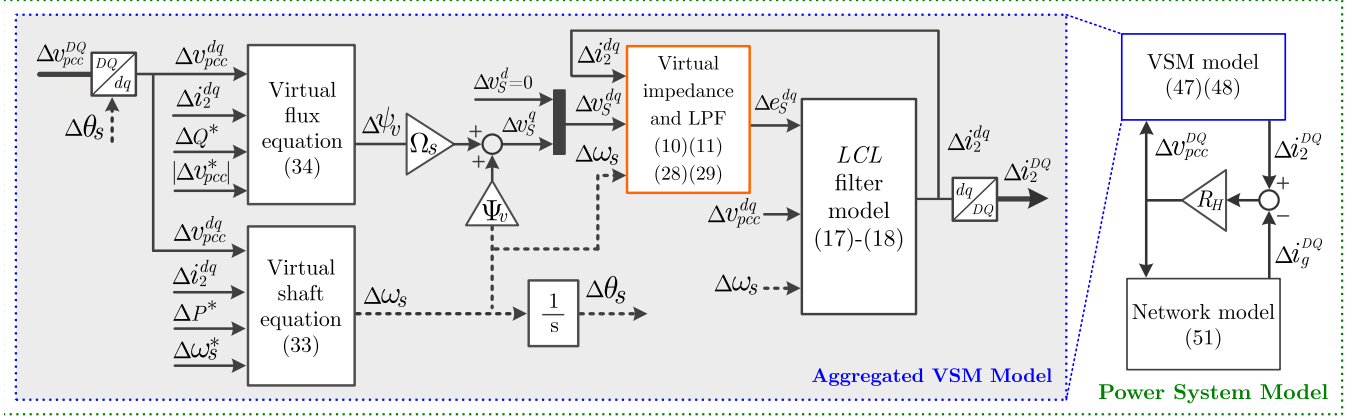


Fig. 3. Block diagram showing the link between the VSM and the network small-signal model. The aggregated model of the VSM includes the *LCL* filter and the control system models.

The aggregated small-signal model of the VSM is

$$\begin{aligned} \frac{d}{dt} \Delta x_{syn} &= A_{syn} \Delta x_{syn} + B_{syn}^{pcc} \Delta v_{pcc}^{DQ} + B_{syn}^{PQ} \Delta P Q^* \\ &\quad + B_{syn}^{\omega} \Delta \omega_s^* + B_{syn}^{|v|} |\Delta v_{pcc}^*| \end{aligned} \quad (50)$$

$$\Delta i_2^{DQ} = C_{syn} \Delta x_{syn} \quad (51)$$

with

$$A_{syn} = \begin{bmatrix} A_f & B_f^S C_c^S + B_{pcc}^{pcc} R_V C_c^{\theta} \\ B_c^i C_{L2} & A_c + B_c^{pcc} R_V C_c^{\theta} \end{bmatrix}, \quad B_{syn}^{PQ} = \begin{bmatrix} 0 \\ B_c^{PQ} \end{bmatrix} \quad (52)$$

$$B_{syn}^{pcc} = \begin{bmatrix} B_f^{pcc} R_S^{-1} \\ B_c^{pcc} R_S^{-1} \end{bmatrix}, \quad B_{syn}^{\omega} = \begin{bmatrix} 0 \\ B_c^{\omega} \end{bmatrix}, \quad B_{syn}^{|v|} = \begin{bmatrix} 0 \\ B_c^{|v|} \end{bmatrix} \quad (53)$$

where $\Delta x_{syn} = [\Delta x_f \ \Delta x_c]'$ and $C_{syn} = [R_S C_{L2} \ R_V C_c^{\theta}]$.

G. Power System Modeling

For simplicity, it was considered the converter is connected to the grid via a long line and the equivalent grid model $Z_{g(s)} \approx R_g + L_{gs}$ is used. However, this linearization and state-space representation can be applied to more complex grid models that consider the power network topology and the dynamic properties of other power converters connected.

The grid model can be linearized and represented as a state-space model, yielding

$$\frac{d}{dt} \Delta i_g^{DQ} = A_g \Delta i_g^{DQ} + B_g^{pcc} \Delta v_{pcc}^{DQ} + B_g^g \Delta v_g^{DQ} \quad (54)$$

with

$$\begin{aligned} A_g &= \begin{bmatrix} -R_g & \Omega_g \\ \frac{L_g}{L_g} & -R_g \\ -\Omega_g & \frac{L_g}{L_g} \end{bmatrix}, \quad B_g^{pcc} = \begin{bmatrix} \frac{1}{L_g} & 0 \\ 0 & \frac{1}{L_g} \end{bmatrix} \\ B_g^g &= \begin{bmatrix} -1 & 0 \\ \frac{L_g}{L_g} & -1 \end{bmatrix} \end{aligned} \quad (55)$$

where i_g is the grid current.

Both the VSM and grid models consider the PCC voltage as an input, however, this variable has not been properly defined. In order to have a feasible numerical solution, a virtual resistor R_H should be assumed between the PCC and ground [33]

$$\Delta v_{pcc}^{DQ} = R_H (\Delta i_2^{DQ} - \Delta i_g^{DQ}) \quad (56)$$

where R_H is the aforementioned virtual resistor. If the value of the virtual resistor is sufficiently large, it would have a minimum impact on the model dynamic and stability properties.

By substituting (56) into (50) and (54), the grid and the VSM models can be connected, yielding

$$\frac{d}{dt} \begin{bmatrix} \Delta x_{syn}^{DQ} \\ \Delta i_g^{DQ} \end{bmatrix} = A_N \begin{bmatrix} \Delta x_{syn}^{DQ} \\ \Delta i_g^{DQ} \end{bmatrix} + B_N^* \begin{bmatrix} \Delta P Q^* \\ \Delta \omega_s^* \\ |\Delta v_{pcc}^*| \end{bmatrix} + B_N^d \Delta v_g^{DQ} \quad (57)$$

$$\Delta i_2^{DQ} = \underbrace{[C_{syn} \ 0]}_{C_N} \begin{bmatrix} \Delta x_{syn}^{DQ} \\ \Delta i_g^{DQ} \end{bmatrix} \quad (58)$$

where

$$A_N = \begin{bmatrix} A_{syn} + B_{syn}^{pcc} R_H C_{syn} & -B_g^{pcc} R_H \\ B_g^{pcc} R_H C_{syn} & A_g - B_g^{pcc} R_H \end{bmatrix} \quad (59)$$

$$B_N^* = \begin{bmatrix} B_{syn}^{PQ} & B_{syn}^{\omega} & B_{syn}^{|v|} \\ 0 & 0 & 0 \end{bmatrix}, \quad B_N^d = \begin{bmatrix} 0 \\ B_g^g \end{bmatrix}. \quad (60)$$

The state matrices (59) and (60) represent the system dynamics and they are used in Section IV to analyze the dynamic properties of VSMs.

IV. STABILITY ANALYSIS

In this section, a robustness analysis of a VSM against the variations of the grid impedance is presented. Also, the impact of the VSM and virtual impedance parameters on the stability of the VSM under weak grid conditions is evaluated.

A. System Description

The nominal voltage was 400 V, the nominal frequency was 50 Hz, and the converter rated power was 15 kVA. The *LCL* filter values were $L_1 = 2.3$ mH, $C_f = 8.8$ μ F,

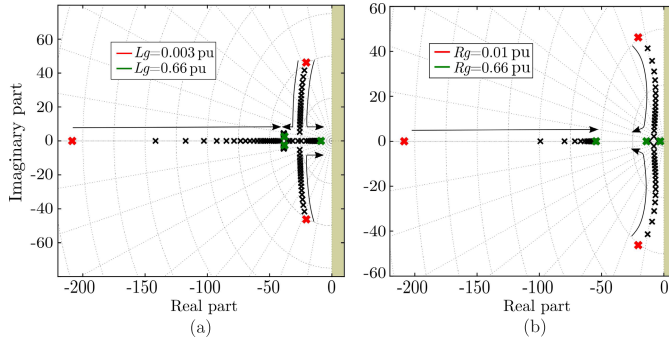


Fig. 4. Closed-loop dominant eigenvalue trajectories when (a) grid inductance (L_g) and (b) grid resistance (R_g).

and $L_2 = 0.93$ mH. The set points were $P^* = 0$ kW, $Q^* = 10$ kVAr, $\omega_s^* = 2\pi 50$ rad/s, and $|v_{pcc}^*| = 400$ V.

B. Nominal Case

VSM robustness against grid inductance (L_g) and resistance (R_g) variations has been studied for zero virtual impedance ($R_V = 0$ pu and $L_V = 0$ pu).

Fig. 4(a) shows the trajectories followed by the dominant eigenvalues when L_g varied between 0.1 mH (0.003 pu) and 22.5 mH (0.66 pu). R_g was 1 mΩ (0.01 pu). When L_g increased, the complex eigenvalues moved in parallel to the imaginary axis until they reached the real axis and became real. Meanwhile, the remaining real eigenvalue moved toward the imaginary axis. Fig. 4(b) shows the eigenvalues trajectories when R_g varied between 1 mΩ (0.01 pu) and 7 Ω (0.66 pu). L_g was 0.1 mH. When R_g increased, the complex eigenvalues moved toward the origin and their natural frequency decreased, approaching the unstable region. These complex eigenvalues reached the real axis and they become real at a point close to the origin. Meanwhile, one of the real eigenvalues moved toward the imaginary axis. It can be seen that the system damping is reduced when L_g and R_g increase. However, this analysis does not provide information on an input (or combination of inputs) that can excite the aforementioned critical modes and produce resonant effects. This issue can be solved by using the SVD analysis.

Fig. 5 shows the frequency response of the maximum SV and how it is related to different inputs of the system. It can be seen that the maximum SV is mainly related to the grid frequency $\Delta\omega_g$ in the low-frequency range. This suggests that the grid frequency disturbances (low-frequency oscillations of $\Delta\omega_g$) have a significant impact on the system stability. Fig. 6(a) shows the frequency response of the maximum SV obtained when L_g increased. The shape of the frequency response changed and, for small values of L_g , the system had two resonances: the synchronous resonance (50 Hz, approx.), and the *LCL* filter resonance (2 kHz). When L_g increased, the gain around the synchronous resonance was attenuated as well as the *LCL* filter resonance gain that also had its frequency (1 kHz) was reduced. Fig. 6(b) shows the frequency response of the maximum SV obtained when R_g increased. The low-frequency range (between 1 and 100 Hz), including

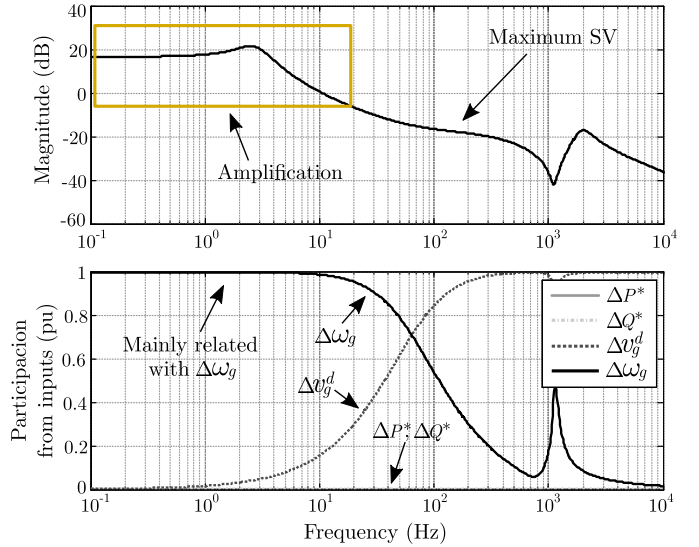


Fig. 5. Frequency response of the maximum SV and the participation of the inputs

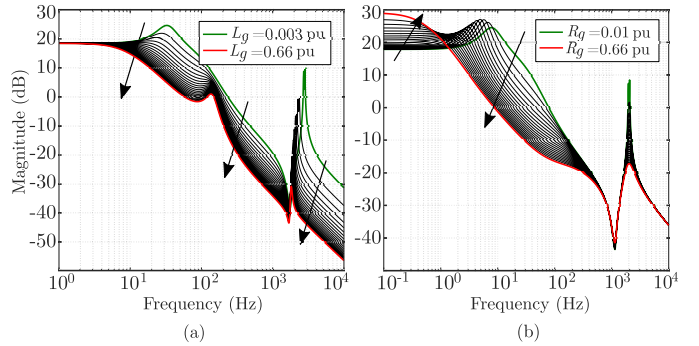


Fig. 6. Frequency response of the maximum SV when (a) grid inductance (L_g) and (b) grid resistance (R_g).

the synchronous resonance, was attenuated while the very low-frequency range (<1 Hz) gain increased 10 dB.

C. Analysis of VSM Parameters

The impact of the VSM parameters on the damping and natural frequency of the dominant eigenvalues was evaluated. Commonly, active and reactive power droops (D_P and D_Q) are determined by the application requirements in order to meet the required steady-state frequency and voltage droop characteristics and, once set, cannot be changed [16], [21], [37], [38]. Therefore, the parameters analyzed were the virtual moment of inertia (J_v) and the reactive power controller gain (K_Q).

Fig. 7(a) shows the trajectories followed by the dominant eigenvalues when J_v varied between 0.02 and 2 and the grid was mainly inductive [$L_g = 6.5$ mH (0.2 pu) and $R_g = 1$ mΩ (0.01 pu)]. When J_v increased, the two real eigenvalues moved in parallel to the real axis until they became complex. Then, they moved toward the origin and their damping and natural frequency were reduced. Also, there was a dominant real eigenvalue that remained in the same position since it was

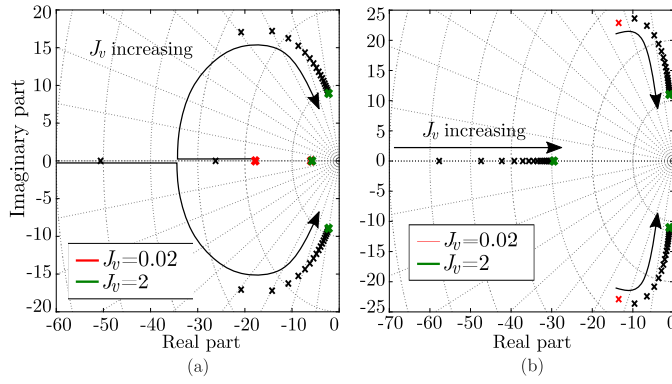


Fig. 7. System dominant eigenvalue trajectories when J_v varied. (a) Grid impedance was mainly inductive. (b) Grid impedance was mainly resistive.

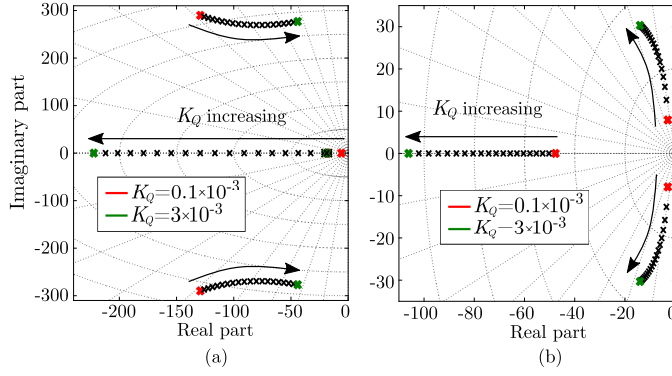


Fig. 8. System dominant eigenvalue trajectories when K_Q varied. (a) Grid impedance was mainly inductive. (b) Grid impedance was mainly resistive.

mainly related to K_Q . Fig. 7(b) shows the trajectory of the dominant eigenvalues when J_v varied and the grid impedance was mainly resistive ($L_g = 0.1$ mH and $R_g = 2\Omega$). When J_v increased, two complex eigenvalues moved rapidly toward the origin, reducing their frequency, and maintaining a similar damping factor.

Fig. 8(a) shows the trajectories followed by the dominant eigenvalues when K_Q changes between 0.1×10^{-3} and 3×10^{-3} . When K_Q increases, the aforementioned dominant real eigenvalue increases its frequency and moves away from the origin. The remaining complex eigenvalues are almost not affected by the variation in K_Q since they are related to J_v . Fig. 8(b) shows the trajectory of the dominant eigenvalues when K_Q varies and the grid impedance is mainly resistive. When K_Q increases, the dominant complex eigenvalues increase their frequency and move away from the unstable region. Also, the real eigenvalue increases its frequency and move away from the unstable region.

For inductive grids, the dominant eigenvalues are mainly linked with J_v and are not affected by variations of K_Q . However, in the case of mainly resistive grid connections, both K_Q and J_v variations affect the dominant eigenvalues.

D. Impact of Virtual Impedance

The impact of the virtual impedance (R_V and L_V) on the dominant eigenvalues was also evaluated. In this analysis, the VSM was connected to a weak grid and these two cases

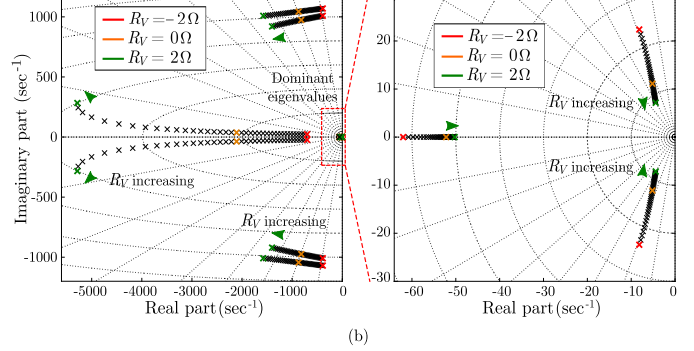
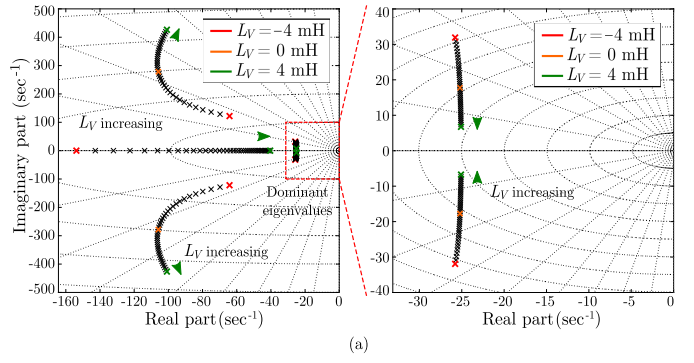


Fig. 9. Trajectories followed by the closed-loop eigenvalues when (a) L_V increases and the grid connection is mainly inductive and (b) R_V increases and the grid connection is mainly resistive.

were considered: mainly inductive weak grid ($L_g = 6.5$ mH and $R_g = 1\text{ m}\Omega$) and mainly resistive weak grid ($L_g = 0.1$ mH and $R_g = 2\Omega$).

Fig. 9(a) shows the trajectories followed by the closed-loop eigenvalues when L_V changed from -4 and 4 mH and the grid connection was mainly inductive. When L_V increased, the dominant eigenvalues moved in parallel to the imaginary axis toward the unstable region, decreasing their frequency and increasing their damping factor. For $L_V \leq 0$ mH, the dominant eigenvalues increased their frequency and decreased their damping factor, mitigating the impact of L_g . However, two medium-frequency eigenvalues reduced their frequency and moved toward the unstable region.

Fig. 9(b) shows the eigenvalue trajectories obtained when R_V changed from -2 and 2 Ω and the grid connection was mainly resistive. When R_V increased, the dominant eigenvalues moved toward the origin, decreasing their frequency and increasing their damping factor. For $R_V \leq 0$ Ω, the dominant eigenvalues increased their frequency and decreased their damping factor, mitigating the impact of R_g . However, four medium-frequency eigenvalues moved toward the unstable region. Therefore, large negative values of R_V can compromise the system stability.

Fig. 10(a) shows the frequency response of the maximum SV obtained when L_V increased and the grid was mainly inductive. Fig. 10(b) shows the frequency response of the maximum VS when R_V varied and the grid was mainly resistive. The shape of the frequency response changed not affected by the variation of L_V and R_V .

Both virtual impedance (R_V and L_V) and grid impedance had a similar impact on the dominant eigenvalues. This result

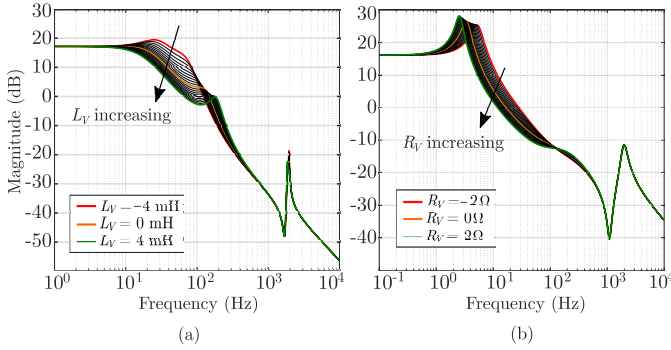


Fig. 10. Frequency response of the maximum SV when (a) grid connection was mainly inductive and the virtual inductance varies (L_V) and (b) grid connection was mainly resistive and virtual resistance varies (R_V).

is consistent with the analysis presented in Section IV-B. The use of a negative virtual impedance can mitigate the impact of the grid impedance, especially under weak grid conditions.

V. VSM AND VIRTUAL IMPEDANCE DESIGN GUIDE

The VSM parameters to be designed are J_v and K_Q , while the virtual impedance parameters are L_V and R_V . The VSM specifications are damping factor ζ and natural frequency ω_n of the dominant eigenvalues.

The design guidelines for the VSM and the virtual impedance parameters include the following procedure.

- 1) Fix the droop coefficients (D_P and D_Q) according to the application requirements in order to have the required steady-state frequency and voltage droop characteristics [16], [21], [37], [38].
- 2) Estimate an approximate equivalent impedance of the power system model (Z_g) and develop the small-signal state-space model presented in (57).
- 3) If possible, design J_v and K_Q to fulfill the specifications. If this condition is met, the virtual impedance is not required ($R_V = 0 \Omega$ and $L_V = 0 \text{ mH}$).
- 4) If the specifications cannot be met, the virtual impedance can be used. For inductive weak grids, use a virtual inductance to increase ($L_V > 0$) or reduce ($L_V < 0$) the effect of the grid impedance. The same procedure can be used for resistive weak grids, but using R_V . One should note that large negative virtual impedance values should be avoided.
- 5) Redesign J_v and K_Q and try to achieve the specifications with the virtual impedance.
- 6) If the specifications cannot be reached by using the virtual impedance, the specifications should be modified (ζ and ω_n). However, for further research purposes, it would be of interest to seek alternative virtual impedance configurations for these cases.

VI. CASE STUDY

The proposed design method was tested by using the following three scenarios.

- 1) Case 1: Mainly inductive grid connection ($L_g = 5.2 \text{ mH}$ and $R_g = 1 \text{ m}\Omega$).
- 2) Case 2: Mainly resistive grid connection ($L_g = 0.1 \text{ mH}$ and $R_g = 4 \Omega$).
- 3) Case 3: Very weak grid connection ($L_g = 22.5 \text{ mH}$ and $R_g = 100 \text{ m}\Omega$).

A. Control System Design

The specifications were $\zeta = \sqrt{2}/2$ and $\omega_n = 35 \text{ rad/s}$. The active and reactive power droop gains were $D_P = 10$ and $D_Q = 50$. The VSM parameters were designed according to the procedure described in Section V for inductive and resistive weak grids.

First, the possibility of achieving the specifications excluding the virtual impedance was tried. The closed-loop eigenvalues of (57) were calculated for different values of J_v and K_Q (see Figs. 7 and 8). The natural frequency and the damping factor of the dominant eigenvalues were plotted in terms of the VSM parameters: $\zeta = f(J_v, K_Q)$ and $\omega_n = f(J_v, K_Q)$. In weak grid scenarios, the original specifications could not be met by adjusting the VSM parameters (as it could be predicted from the analysis presented in Section IV-C).

1) *Case 1 (Mainly Inductive Grid):* The dominant eigenvalues were mainly related to J_v , and the specifications (ζ and ω_n) could not be achieved by tuning only one parameter. Therefore, a virtual impedance was required. The virtual inductance value was set to $L_V = -1.1 \text{ mH}$ and the design process was repeated. The VSM parameters obtained were $J_v = 0.2$ and $K_Q = 1 \times 10^{-3}$.

2) *Case 2 (Mainly Resistive Grid):* The same process was applied. The frequency response specifications could not be achieved by tuning the VSM parameters only and the virtual impedance was also required. In this case, the virtual resistance was set to $R_V = -2 \Omega$. The VSM parameters that satisfied the specifications were $J_v = 0.06$ and $K_Q = 2 \times 10^{-3}$.

3) *Case 3 (Very Weak Grid):* The same process was applied. The high inductance value reduced considerably the frequency of the dominant eigenvalues [see Fig. 4(a)] and the frequency response specifications could not be achieved by tuning the VSM parameters. In this case, a negative virtual inductance was used in order to mitigate the impact of the grid inductance and to increase the frequency of the dominant eigenvalues. The virtual inductance was set to $L_V = -18 \text{ mH}$ and the design process was repeated. The VSM parameters were set to $J_v = 0.02$ and $K_Q = 0.5 \times 10^{-3}$.

B. Small-Signal Model Validation

The accuracy of the developed small-signal model in (57) was validated by comparing the transient responses of linearized and nonlinear models for different grid conditions and different VSM parameters. The nonlinear model with all nonlinear effects was developed in Simulink by using SimPowerSystems Toolbox. The VSCs were modeled as ideal voltage sources in order to avoid the issues related with switching noise and harmonics.

Fig. 11(a) shows the transient responses of the small-signal model and the nonlinear model to a step change of active power reference ΔP^* from 0 to 2 kW when Case 2 was considered. The low-frequency dynamics were well represented by the small-signal model. Fig. 11(b) shows the transient responses of the small-signal model and the nonlinear model to a step change of grid voltage magnitude Δv_g^{DQ} from 1 to 0.8 pu when Case 3 was considered. It can be seen the model represented accurately the dynamics of the model.

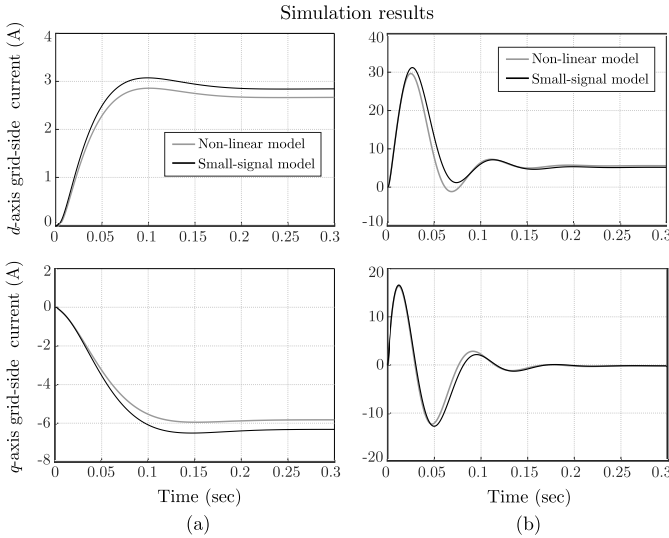


Fig. 11. Comparison between the transient responses of the small-signal model and the nonlinear model for (a) step change of $\Delta P^* = 2$ kW when Case 2 is applied and (b) step change of $\Delta v_g^{DQ} = -0.2$ pu when Case 3 is applied.

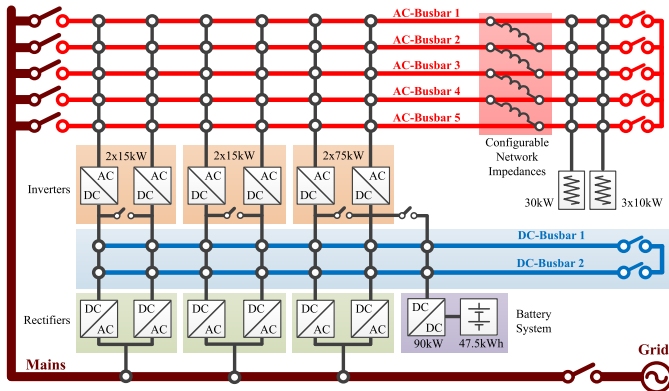


Fig. 12. Electrical diagram of the SEIL.

VII. EXPERIMENTAL VALIDATION

A. Prototype Description

The VSM small-signal model and the conclusions obtained from the eigenvalue analysis were experimentally validated in the Smart Energy Integration Lab (SEIL) [39], [40]. The sampling and switching frequencies were set to 10 kHz and pulsedwidth modulation with third-harmonic injection was used. The controller was implemented on an embedded PC.

Fig. 12 shows the hardware diagram of the SEIL facilities. The VSC1 was connected to ac busbar 5. Busbar 1 was connected to the grid, while Busbars 2–4 were used to introduce the network impedances. Moreover, a rectifier was used to maintain the dc voltage constant. Fig. 13 shows detailed photographs of the main hardware components used in the experimental validation.

B. Small-Signal Model Validation

The VSM and virtual impedance parameters designed in Section VI-A for inductive and resistive grids

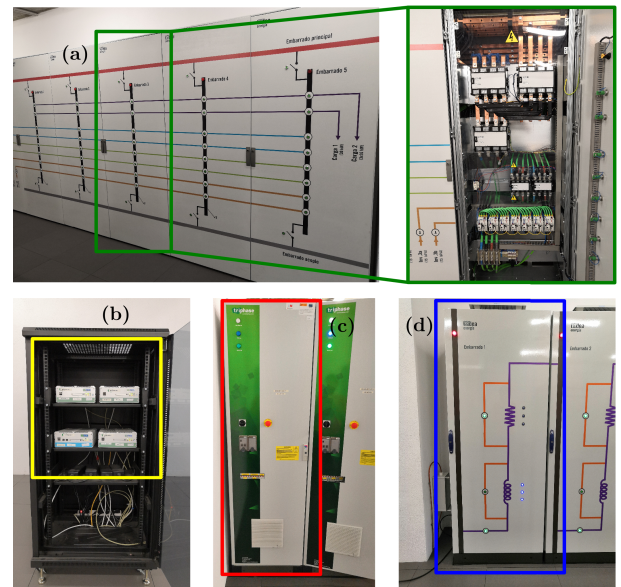


Fig. 13. Photograph of the SEIL facilities. (a) AC-busbars. (b) Embedded PCs. (c) Power converter + rectifier. (d) Configurable network impedances

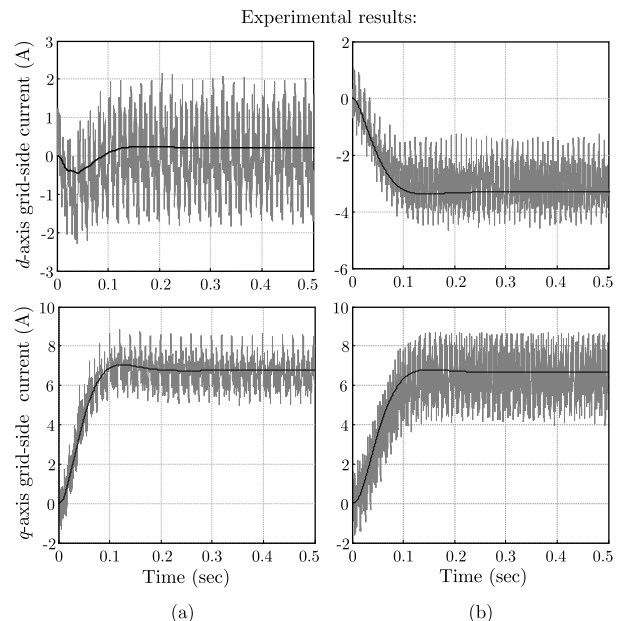


Fig. 14. Experimental results. Transient response of the small-signal model and the hardware prototype to a step change of $\Delta P^* = 3$ kW when (a) grid connection is mainly inductive and (b) grid connection is mainly resistive.

(Case 1 and Case 2) were validated experimentally. Fig. 14(a) and (b) shows the transient responses of the small-signal model and the prototype to a step change of the active power set point, from 0 to 3 kW ($\Delta P^* = 3$ kW). Fig. 14(a) shows the responses for the inductive grid, while Fig. 14(b) shows the responses for the resistive grid. In both cases, $Q^* = 10$ kVAr. The VSM dynamics are well represented by the proposed model and the frequency response specifications set at the design step were achieved. The current contained some harmonic distortion and high-frequency ripple because of the modulation process that cannot be predicted

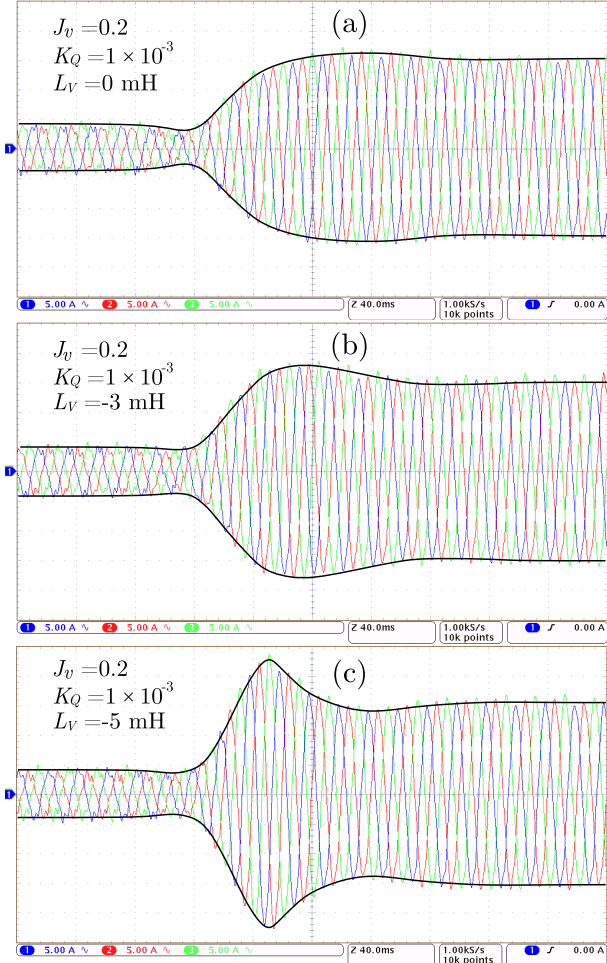


Fig. 15. Experimental results. Transient response of the hardware prototype when the grid was mainly inductive and different values of the virtual inductance were used. (a) $L_V = 0$ mH. (b) $L_V = -3$ mH. (c) $L_V = -5$ mH.

by the small-signal model. There are several methods to deal with power quality issues in VSMs and to reduce the harmonic distortion [32]. However, these methods modify the dynamic properties of the VSM and may influence the stability analysis. For that reason, no harmonic control has been applied in this paper.

C. VSM and Negative Virtual Impedance Validation

Fig. 15 shows the transient response when the grid was mainly inductive (Case 1— $L_g = 5.21$ mH and $R_g = 1$ mΩ) and a step change of P^* from 0 to 5 kVAr was applied. The reactive power set point and the virtual resistance were set to $Q^* = 5$ kVAr and $R_V = 0$ Ω. Three different virtual inductance values were used. Fig. 15(a) shows the transient response with a virtual $L_V = 0$ mH, which can be considered as the natural response of the VSM. Fig. 15(b) and (c) shows the transient responses with $L_V = -3$ mH and $L_V = -5$ mH, respectively. It can be seen that the added negative virtual impedance increased the frequency and reduced the damping factor of the dominant eigenvalues, obtaining a faster and less damped transient response. This result is consistent with the analysis presented in Section IV-D.

Fig. 16(a)–(c) shows a comparison of the VSM performance when the grid was mainly inductive (Case 1) and the virtual moment of inertia (J_v) was set to $J_v = 0.2$, $J_v = 0.05$, and $J_v = 0.01$, respectively. The remaining VSM and virtual impedance parameters were set to $K_Q = 0.001$, $L_V = 0$ H, and $R_V = 0$ Ω. It can be seen that reducing the virtual moment of inertia leads to the damping factor increase and the reduction of the frequency of the dominant eigenvalues. This result is consistent with the analysis presented in Section IV-C.

Fig. 16(d)–(f) shows a comparison of the VSM performance when the grid was mainly inductive (Case 1) and the virtual inductance (L_V) was set to $L_V = -2$ mH, $L_V = -4$ mH, and $L_V = -6$ mH, respectively. The remaining VSM and virtual impedance parameters were set to $J_v = 0.2$, $K_Q = 0.001$, and $R_V = 0$ Ω. It can be seen that decreasing the virtual inductance (negative values) reduces the damping factor and increases the frequency of the dominant eigenvalues, mitigating the impact of the grid impedance. Therefore, by using a negative virtual inductance, it is possible to obtain a faster (and less damped) transient response compared to the use of the VSM parameters only. This result is consistent with the analysis presented in Section IV-D.

VIII. DISCUSSION

An accurate small-signal modeling and control design procedure for VSM-based VSC with virtual impedance has been presented in this paper. The VSM was modeled in detail and the impacts of the grid impedance, the VSM parameters, and the virtual impedance on the system stability were evaluated. The VSM stability limits have been analytically sought and the possible benefits of using the virtual impedance under (extremely) weak grid conditions have been identified. The principal results are summarized in the following.

- 1) The impact of the grid impedance (inductance and resistance) on the small-signal model has been evaluated. The analysis presented in Section IV-B revealed that the VSM is robust against large variations of the grid inductance values. However, weak resistive grids have a more negative impact and the dominant eigenvalues tend to move faster toward the unstable region. Moreover, the influence of the VSM parameters on the dominant eigenvalues has been analyzed for different grid conditions. It has been shown that, depending on the network conditions, only the use of J_v and K_Q may be insufficient to achieve the desired frequency response specifications.
- 2) Compared to other control strategies proposed in the literature to facilitate the integration of RES to distribution networks, the VSM has become an attractive solution since the power systems are designed to operate with conventional synchronous generators. Typically, conventional control schemes for microgrid operation use local current and/or voltage controllers and droop-based primary controllers [8]–[10]. However, conventional control approaches have certain limitations and, especially in the

Experimental results

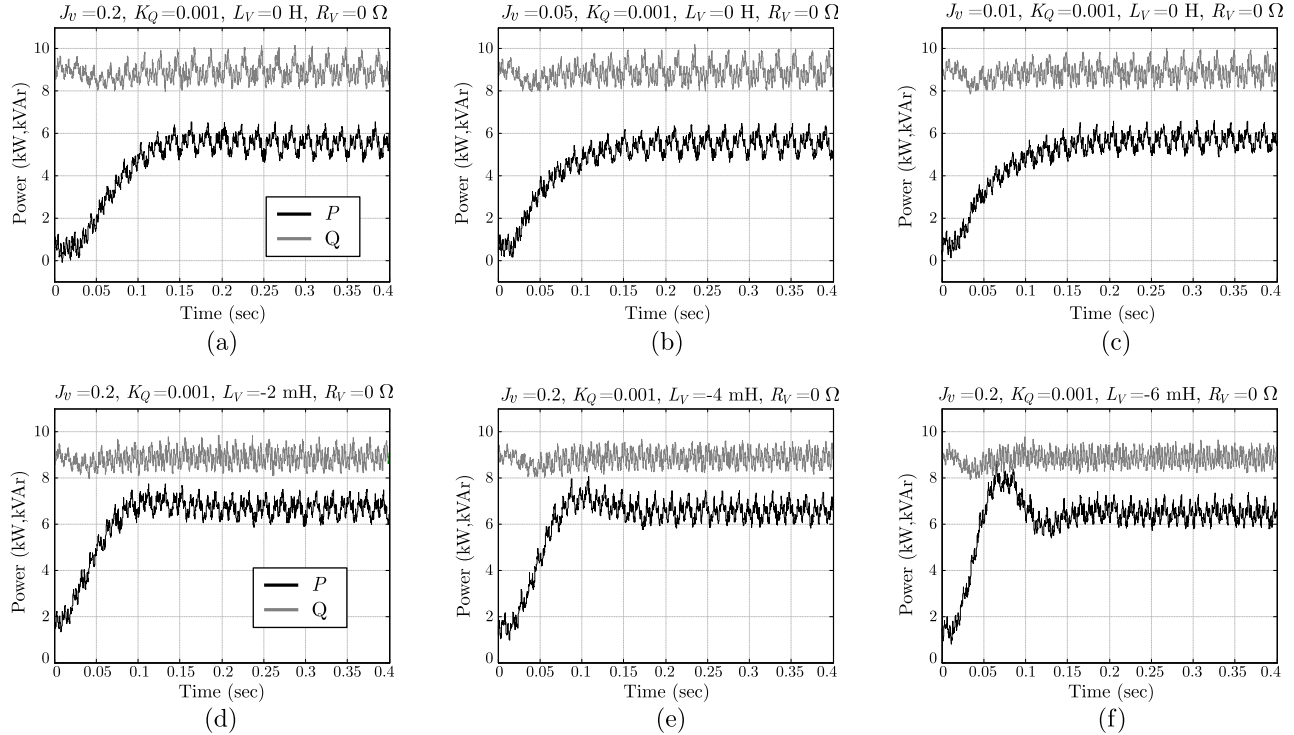


Fig. 16. Experimental results. Transient response of the prototype when the grid was mainly inductive and a step change of P^* was applied. (a) $J_v = 0.2$ and excluding the virtual impedance. (b) $J_v = 0.05$ and excluding the virtual impedance. (c) $J_v = 0.01$ and excluding the virtual impedance. (d) $J_v = 0.2$ and including virtual inductance $L_V = -2$ mH. (e) $J_v = 0.2$ and including virtual inductance $L_V = -4$ mH. (f) $J_v = 0.2$ and including virtual inductance $L_V = -6$ mH.

case of large values of grid impedances, cannot ensure the system stability and control performance.

IX. CONCLUSION

VSMs have become commonly used to integrate RESs to weak grids as they can provide virtual inertia and voltage support. However, weak grid conditions deteriorate VSM dynamic response. In this paper, a detailed modeling and design procedure for VSMs with virtual impedances was proposed. The system was modeled in detail and then linearized. The eigenvalue analysis revealed that VSMs can withstand large grid inductance variations, but resistive grids can jeopardize closed-loop stability. Also, the SVD analysis revealed that the synchronous resonance is attenuated in weak grid scenarios (both inductive and resistive). Theoretical analyzes revealed that virtual impedance can help to improve the transient response. Moreover, it has been shown that virtual inductance and resistance can take negative values that help in canceling the weak grid effects. The small-signal analysis was an effective tool for predicting the low-frequency dynamics of a VSM, as shown in the experimental validation. All the control system developments were validated on a 15-kVA prototype of a VSM connected to a configurable weak grid.

REFERENCES

- [1] B. Wen, R. Burgos, D. Boroyevich, P. Mattavelli, and Z. Shen, "AC stability analysis and dq frame impedance specifications in power-electronics-based distributed power systems," *IEEE J. Emerg. Sel. Topics Power Electron.*, vol. 5, no. 4, pp. 1455–1465, Dec. 2017.
- [2] A. Adib, B. Mirafzal, X. Wang, and F. Blaabjerg, "On stability of voltage source inverters in weak grids," *IEEE Access*, vol. 6, pp. 4427–4439, 2018.
- [3] R. Majumder, "Some aspects of stability in microgrids," *IEEE Trans. Power Syst.*, vol. 28, no. 3, pp. 3243–3252, Aug. 2013.
- [4] X. Chen, C. Y. Gong, H. Z. Wang, and L. Cheng, "Stability analysis of LCL-type grid-connected inverter in weak grid systems," in *Proc. ICRERA*, Nov. 2012, pp. 1–6.
- [5] S. M. Ashabani and Y. A.-R. I. Mohamed, "A flexible control strategy for grid-connected and islanded microgrids with enhanced stability using nonlinear microgrid stabilizer," *IEEE Trans. Smart Grid*, vol. 3, no. 3, pp. 1291–1301, Sep. 2012.
- [6] Y. Yan, D. Shi, D. Bian, B. Huang, Z. Yi, and Z. Wang, "Small-signal stability analysis and performance evaluation of microgrids under distributed control," *IEEE Trans. Smart Grid*, to be published.
- [7] Y. Zhang, L. Xie, and Q. Ding, "Interactive control of coupled microgrids for guaranteed system-wide small signal stability," *IEEE Trans. Smart Grid*, vol. 7, no. 2, pp. 1088–1096, Mar. 2016.
- [8] J. M. Guerrero, J. C. Vasquez, J. Matas, L. G. de Vicuna, and M. Castilla, "Hierarchical control of droop-controlled AC and DC microgrids—A general approach toward standardization," *IEEE Trans. Ind. Electron.*, vol. 58, no. 1, pp. 158–172, Jan. 2011.
- [9] J. M. Guerrero, M. Chandorkar, T.-L. Lee, and P. C. Loh, "Advanced control architectures for intelligent microgrids—Part I: Decentralized and hierarchical control," *IEEE Trans. Ind. Electron.*, vol. 60, no. 4, pp. 1254–1262, Apr. 2013.
- [10] H. R. Baghaee, M. Mirsalim, and G. B. Gharehpetian, "Power calculation using RBF neural networks to improve power sharing of hierarchical control scheme in multi-DER microgrids," *IEEE J. Emerg. Sel. Topics Power Electron.*, vol. 4, no. 4, pp. 1217–1225, Dec. 2016.
- [11] J. W. Simpson-Porco, Q. Shafiee, F. Dörfler, J. C. Vasquez, J. M. Guerrero, and F. Bullo, "Secondary frequency and voltage control of islanded microgrids via distributed averaging," *IEEE Trans. Ind. Electron.*, vol. 62, no. 11, pp. 7025–7038, Nov. 2015.
- [12] X. Wu, C. Shen, and R. Iravani, "A distributed, cooperative frequency and voltage control for microgrids," *IEEE Trans. Smart Grid*, vol. 9, no. 4, pp. 2764–2776, Jul. 2018.

- [13] F. Guo, C. Wen, J. Mao, and Y. D. Song, "Distributed secondary voltage and frequency restoration control of droop-controlled inverter-based microgrids," *IEEE Trans. Ind. Electron.*, vol. 62, no. 7, pp. 4355–4364, Jul. 2015.
- [14] Y. Han, H. Li, P. Shen, E. A. A. Coelho, and J. M. Guerrero, "Review of active and reactive power sharing strategies in hierarchical controlled microgrids," *IEEE Trans. Power Electron.*, vol. 32, no. 3, pp. 2427–2451, Mar. 2017.
- [15] Q.-C. Zhong and G. Weiss, "Synchronverters: Inverters that mimic synchronous generators," *IEEE Trans. Ind. Electron.*, vol. 58, no. 4, pp. 1259–1267, Apr. 2011.
- [16] S. Dong and Y. C. Chen, "Adjusting synchronverter dynamic response speed via damping correction loop," *IEEE Trans. Energy Convers.*, vol. 32, no. 2, pp. 608–619, Jun. 2017.
- [17] Z. Ma and Q.-C. Zhong, "Synchronverter-based control strategy for back-to-back converters in wind power applications," *IFAC Proc. Vols.*, vol. 45, no. 21, pp. 349–354, 2012.
- [18] R. Aouini, B. Marinescu, K. Ben Kilani, and M. Elleuch, "Stability improvement of the interconnection of weak AC zones by synchronverter-based HVDC link," *Electr. Power Syst. Res.*, vol. 142, pp. 112–124, Jan. 2017.
- [19] V. Natarajan and G. Weiss, "Synchronverters with better stability due to virtual inductors, virtual capacitors, and anti-windup," *IEEE Trans. Ind. Electron.*, vol. 64, no. 7, pp. 5994–6004, Jul. 2017.
- [20] D. Chen, Y. Xu, and A. Q. Huang, "Integration of DC microgrids as virtual synchronous machines into the AC grid," *IEEE Trans. Ind. Electron.*, vol. 64, no. 9, pp. 7455–7466, Sep. 2017.
- [21] Z. K. Shuai, Y. Hu, Y. L. Peng, C. Tu, and Z. J. Shen, "Dynamic stability analysis of synchronverter-dominated microgrid based on bifurcation theory," *IEEE Trans. Ind. Electron.*, vol. 64, no. 9, pp. 7467–7477, Sep. 2017.
- [22] J. Roldán-Pérez, M. Prodanovic, and A. Rodríguez-Cabero, "Detailed discrete-time implementation of a battery-supported synchronverter for weak grids," in *Proc. IECON*, Oct./Nov. 2017, pp. 1083–1088.
- [23] X. Wang, Y. W. Li, F. Blaabjerg, and P. C. Loh, "Virtual-impedance-based control for voltage-source and current-source converters," *IEEE Trans. Power Electron.*, vol. 30, no. 12, pp. 7019–7037, Dec. 2015.
- [24] J. M. Guerrero, J. Matas, L. G. de Vicuña, M. Castilla, and J. Miret, "Decentralized control for parallel operation of distributed generation inverters using resistive output impedance," *IEEE Trans. Ind. Electron.*, vol. 54, no. 2, pp. 994–1004, Apr. 2007.
- [25] H. Wang, M. Han, R. Han, J. M. Guerrero, and J. C. Vasquez, "A decentralized current-sharing controller endows fast transient response to parallel DC–DC converters," *IEEE Trans. Power Electron.*, vol. 33, no. 5, pp. 4362–4372, May 2018.
- [26] A. D. Paquette and D. M. Divan, "Virtual impedance current limiting for inverters in microgrids with synchronous generators," *IEEE Trans. Ind. Appl.*, vol. 51, no. 2, pp. 1630–1638, Mar. 2015.
- [27] H. Wang, Y. Chen, and Y.-F. Liu, "A passive-impedance-matching technology to achieve automatic current sharing for a multiphase resonant converter," *IEEE Trans. Power Electron.*, vol. 32, no. 12, pp. 9191–9209, Dec. 2017.
- [28] J. A. Suul, S. D'Arco, and G. Guidi, "Virtual synchronous machine-based control of a single-phase bi-directional battery charger for providing vehicle-to-grid services," *IEEE Trans. Ind. Appl.*, vol. 52, no. 4, pp. 3234–3244, Jul./Aug. 2016.
- [29] P. Piya and M. Karimi-Ghartemani, "A stability analysis and efficiency improvement of synchronverter," in *Proc. APEC*, Mar. 2016, pp. 3165–3171.
- [30] J. L. Agorreta, M. Borrega, J. López, and L. Marroyo, "Modeling and control of N -paralleled grid-connected inverters with LCL filter coupled due to grid impedance in PV plants," *IEEE Trans. Power Electron.*, vol. 26, no. 3, pp. 770–785, Mar. 2011.
- [31] H. Akagi, Y. Kanazawa, and A. Nabae, "Instantaneous reactive power compensators comprising switching devices without energy storage components," *IEEE Trans. Ind. Appl.*, vol. IA-20, no. 3, pp. 625–630, May 1984.
- [32] J. Roldán-Pérez, A. Rodríguez-Cabero, and M. Prodanović, "Harmonic virtual impedance design for parallel-connected grid-tied synchronverters," *IEEE J. Emerg. Sel. Topics Power Electron.*, vol. 7, no. 1, pp. 493–503, Mar. 2018.
- [33] N. Pogaku, M. Prodanovic, and T. C. Green, "Modeling, analysis and testing of autonomous operation of an inverter-based microgrid," *IEEE Trans. Power Electron.*, vol. 22, no. 2, pp. 613–625, Mar. 2007.
- [34] W. S. Levine, *The Control Systems Handbook: Control System Advanced Methods*, 2nd ed. Boca Raton, FL, USA: CRC Press, 2009.
- [35] A. Rodríguez-Cabero, M. Prodanovic, and J. Roldán-Pérez, "Analysis of dynamic properties of VSCs connected to weak grids including the effects of dead-time and time delays," *IEEE Trans. Sustain. Energy*, to be published.
- [36] A. Rodríguez-Cabero and M. Prodanovic, "Stability analysis for weak grids with power electronics interfaces," in *Proc. IECON*, Oct. 2016, pp. 2402–2407.
- [37] S. Dong and Y. C. Chen, "A method to directly compute synchronverter parameters for desired dynamic response," *IEEE Trans. Energy Convers.*, vol. 33, no. 2, pp. 814–825, Jun. 2018.
- [38] H. Wu *et al.*, "Small-signal modeling and parameters design for virtual synchronous generators," *IEEE Trans. Ind. Electron.*, vol. 63, no. 7, pp. 4292–4303, Jul. 2016.
- [39] M. Prodanovic, A. Rodríguez-Cabero, M. Jiménez-Carrizosa, and J. Roldán-Pérez, "A rapid prototyping environment for DC and AC microgrids: Smart energy integration lab (SEIL)," in *Proc. ICDCM*, Jun. 2017, pp. 421–427.
- [40] F. Huerta, J. K. Gruber, M. Prodanovic, and P. Matatagui, "Power-hardware-in-the-loop test beds: Evaluation tools for grid integration of distributed energy resources," *IEEE Ind. Appl. Mag.*, vol. 22, no. 2, pp. 18–26, Mar./Apr. 2016.



Alberto Rodríguez-Cabero received the Degrees in industrial technical engineering and industrial engineering, specialized in electronics, and the master's degree in research in engineering systems modeling from Comillas Pontifical University, Madrid, Spain, in 2011, 2013, and 2016, respectively.

From 2014 to 2015, he was a Control Engineer with the Institute for Research in Technology (IIT), Comillas Pontifical University. Since 2015, he has been with the Electrical Systems Unit, IMDEA Energy Institute, Madrid. His current research interests include the design and control of power electronics converters, power quality, and microgrids.



Javier Roldán-Pérez (S'12–M'14) received the B.S. degree in industrial engineering, the M.S. degree in electronics and control systems, the M.S. degree in system modeling, and the Ph.D. degree in power electronics from Comillas Pontifical University, Madrid, Spain, in 2009, 2010, 2011, and 2015, respectively.

From 2010 to 2015, he was with the Institute for Research in Technology (IIT), Comillas Pontifical University. He was a Visiting Ph.D. Student with the Department of Energy Technology, Aalborg University, in 2014. From 2015 to 2016, he was with the Electric and Control Systems Department, Norvento Energía Distribuida, Madrid. In 2016, he joined the Electrical Systems Unit, IMDEA Energy Institute, Madrid, where his research topics are the integration of renewable energies, microgrids, and power electronics applications.



Milan Prodanovic (M'01) received the B.Sc. degree in electrical engineering from the University of Belgrade, Belgrade, Serbia, in 1996, and the Ph.D. degree from Imperial College London, London, U.K., in 2004.

From 1997 to 1999, he was with GVS Engineering Company, Belgrade, where he developing uninterruptible power system (UPS) systems. From 1999 to 2010, he was a Research Associate of electrical and electronic engineering with Imperial College London. He is currently a Senior Researcher and the Head of the Electrical Systems Unit, IMDEA Energy Institute, Madrid, Spain. His current research interests include the design and control of power electronics interfaces for distributed generation, microgrids control, and active management of distribution networks.